Published in : Journal of Structural Engineering (2023), vol. 149, n°04
DOI: 10.1061/JSENDH.STENG-11642
Status : Postprint (Author's version)

Experimental and Numerical Investigations on Closely Spaced Built-Up Angle Members

Loris Saufnay[1]; André Beyer[2]; Jean-Pierre Jaspart[3]; and Jean-François Demonceau[4]

[1] Teaching Assistant and Ph.D. Candidate, Urban & Environmental Engineering (UEE) Dept., Univ. of Liège, All. de la Découverte b52, Liège 4000, Belgium (corresponding author). ORCID: https://orcid.org/0000-0001-5347-0573.
[2] Research Engineer, Steel Construction Division, Centre Technique Industriel de la Construction Métallique, Espace Technologique l'Orme des Merisiers—Bâtiment Apollo,Saint-Aubin 91190, France.
[3] Full Professor, Urban & Environmental Engineering (UEE) Dept., Univ. of Liège, All. de la Découverte b52, Liège 4000, Belgium.
[4] Associate Professor, Urban & Environmental Engineering (UEE) Dept., Univ. of Liège, All. de la Découverte b52, Liège 4000, Belgium. ORCID: https://orcid.org/0000-0002-0988-8929.

Abstract

This paper presents the results of 10 laboratory tests performed on closely spaced built-up members fabricated from hot-rolled angle sections. Such members are of special interest in the construction and reinforcement of steel lattice towers used for telecommunication or electrical transmission lines. The angle sections used in this study were star-battened with pinned support conditions. In particular, two configurations were studied: star-battened angles with equal sections (SBE) (composed of two chords with the same section), and star-battened angles with unequal sections (SBU) (composed of two chords with different sections). The influence of connection spacing along the members and different types of connections (fully preloaded bolts, partially preloaded bolts) were also studied. In addition, the important influence of geometric imperfections on failure load and failure mode were analyzed. In this paper, a numerical model is introduced after the laboratory tests are presented. The model was built in ANSYS version 18.2 and was validated based on the results obtained during the experimental campaign. The numerical results highlighted the sensitivity of failure modes to initial imperfections (out-of-straightness, load eccentricity). Last, the validated numerical model is thought to be used in a wider parametric study with the aim of developing new design recommendations.

Keywords :

Laboratory tests

Built-up members

Angle sections

Lattice towers

Introduction

Lattice towers are commonly built to carry high voltage electric power lines or to support antennas for telecommunication, as shown in **Fig. 1**.

In most cases, such structures are fabricated of steel single or built-up sections, which present several advantages. Angle sections for lattice towers are easy to manufacture because of quick factory setup, and designs can be adjusted to resist various service loads (for instance, modifying the cable configuration for overhead line towers). Due to their small size and low weight, the transportation of the various elements is quite easy. In addition, the overall weight of a steel lattice structure is generally less than that of other types of tower structures, resulting in raw material savings for its concrete foundation. Thanks to these material savings, construction costs are lower than those for a free-standing tubular tower with similar stiffness. Last, the transparency of lattice towers leads to a relatively limited impact on the landscape.

For the construction of new towers, single angles are generally preferred to built-up members. However, if an existing tower needs reinforcement, adding a second angle section to create a built-up member is an effective means to increase load-carrying capacity for a relatively low cost. The need to reinforce may arise from additional loads that have to be carried—for example, loads resulting from the installation of additional antennas. Currently, the deployment of 5th generation (5G) is increasing the need to add antennas, and consequently, the need to reassess existing towers; in some instances, this results in the need for reinforcement. The need to reinforce may also result from the aging of existing members due to corrosion, because it reduces the area of the angle sections resisting applied loads. The residual resistance of partially corroded angle sections was studied by Oszvald et al. (2016). They found that, depending on certain parameters—such as the distribution of the corrosion over the member length or thickness reduction— the remaining load-bearing capacity may be satisfactory. However, if this is not the case, the tower has to be reinforced.

There are several possible ways to reinforce a tower. In recent years, the possibility of strengthening steel members with carbon fiber–reinforced polymers (CFRP) has been studied (Elchalakani 2016; Selvaraj et al. 2016; Tomasz and Siwowski 2016; Vlachakis et al. 2021; Wan et al. 2016; Yousefi et al. 2021). Nonetheless, even if this innovative strengthening method is promising for steel member retrofitting, its application on-site appears to be complicated. Moreover, further investigation is needed regarding whether CFRP may be applied on galvanized surfaces. The technique of reinforcing by placing an additional angle section is currently much more widely practiced. **Fig. 2** illustrates such reinforcement on an existing telecommunication tower. The tower is strengthened by creating a star-battened leg. The batten plates are bolted to both angle sections. The use of welded built-up sections is an alternative (Botelho et al. 2019; Yu et al. 2017). Nonetheless, due to the difficulty of welding on-site, this type of built-up member is more suited for new towers.

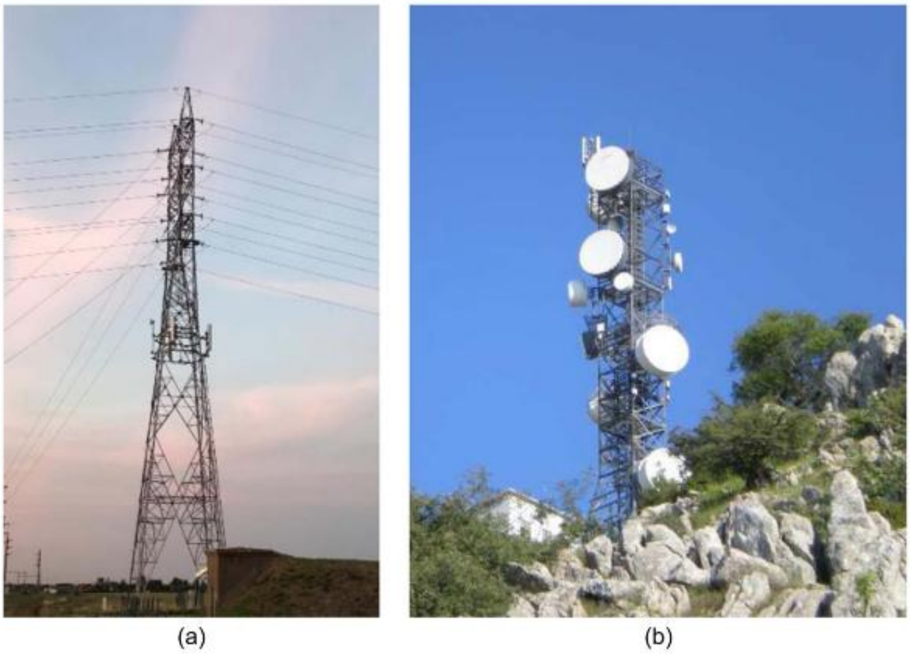

Fig. 1. Lattice tower (a) for electrical transmission lines; and (b) for telecommunication.

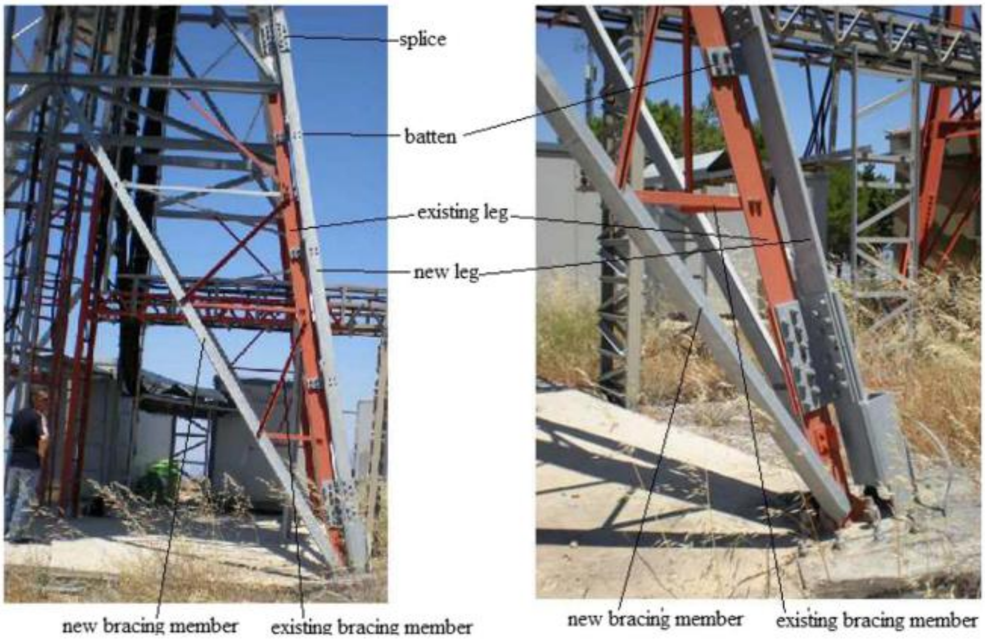

Fig. 2. Reinforcement of telecommunication towers using a star-battened angle section leg.

The resistance of built-up members has been regularly studied for a long time. Theoretical studies started with Timošenko (1961). However, these studies focused on the resistance of battened columns, that is, built-up members with much higher distances between the chords than in the members considered in this study. The general theory may be applied to investigate the resistance of closely spaced built-up members, but the specific influence of the connections needs to be accounted for. Several experimental studies have been performed to assess the exact effect of the connections on the resistance of closely spaced built-up members. Kitipornchai and Lee (1986) conducted 54 tests on angle and T-section members; this included 2 × 8 tests on back-to-back connected angle sections (each test was performed twice). In Kitipornchai and Lee's (1986) study, each built-up specimen had two intermediate connections. Consequently, the influence of connection spacing, which is an important parameter for the resistance of built-up members (Timošenko 1961; Timoshenko 1913), has not been studied. In addition, Kitipornchai and Lee's (1986) study only concerned back-to-back specimens. But for the reinforcement of tower leg members, the star-battened configuration is of special interest and needs to be studied. Stainless steel columns were studied in part by Botelho et al. (2019). They reported on a test on a star-battened angle section member with identical chords subjected only to an axial force. The two intermediate connections were made with welds. Consequently, this typology was not well-suited for tower reinforcements on-site. Still, the research work performed is of high interest, because it was demonstrated that the current Eurocode 3 approach [EN 1993-1-1 (CEN 2005a); EN 1993-1-4 (CEN 2005b)] is very conservative. Therefore, supplementary investigations are required to improve the existing rules. Other previous research by Lu et al. (2015) and Mills et al. (2012) focused specifically on the resistance of legs reinforced by adding a second angle section, creating a star-battened built-up member. These two studies characterized the load transfer mechanism from the unreinforced part of the leg to the reinforced part. Moreover, the influence of an existing preloading in the leg member was studied. It was found that a minimum reinforcement length is necessary in order for the additional angle section to be fully active and carry 50% of the applied loading. These two studies did not, however, address the design of built-up members; rather, they focused on the experimental characterization of the load transfer mechanism and its representation in numerical modeling.

This literature review shows that closely spaced built-up members made of angles are widely used in civil engineering. However, the stability behavior of such members is not completely understood, and there is a lack of consistent design rules in the standards. Accordingly, this study aimed to investigate experimentally and numerically the stability of closely spaced built-up members to improve the existing design rules in Eurocode 3 Part 1-1 [EN 1993-1-1 (CEN 2005a)] concerning this particular type of structural member. This paper presents experimental investigations carried out at the University of Liège and numerical simulations performed in ANSYS version 18.2. The experimental and numerical investigations were part of the European Research Fund for Coil and Steel (RFCS) project ANGELHY, which aimed to provide innovative reinforcement solutions for telecommunication and transmission lattice towers. The experimental campaign consisted of 10 laboratory tests on closely spaced built-up members in two configurations—star-battened angles with equal sections (SBE), and star-battened angles with unequal sections (SBU). The numerical model accounts for geometrical and material properties as well as the full non-linear material law [geometrically and materially nonlinear analysis (GMNIA) simulations] to analyze the tests further on. The specimen sections are represented in **Fig. 3**.

Published in : Journal of Structural Engineering (2023), vol. 149, n°04
DOI: 10.1061/JSENDH.STENG-11642
Status : Postprint (Author's version)

Experimental Investigations

TESTED SPECIMENS

The various specimens in the two tested configurations were chosen considering the limitations of the test rig and the results of preliminary numerical simulations. Endplates were welded at the ends of the specimens; this helped to position the specimens at the right place in the test machine. The parameters studied in the experimental campaign were principally member slenderness and the level of bolt preloading in the connections. However, the laboratory tests also revealed the significant influence of initial geometric imperfections (see "Numerical Results—Validation of the Finite-Element Model").

Each specimen was manufactured from two angle profiles jointed with several batten plates and bolts [M16 of class 10.9 or M12 of class 10.9 according to EN 14399-3 (CEN 2015)]. All specimens were fabricated from grade S355 steel (yield strength ¼ 355 MPa); the batten plates were fabricated from lower-grade steel.

Most of the specimens were tested with pinned support conditions at their extremities about both bending axes, because this study aimed to understand the stability behavior of star-battened members with pinned support conditions as a limit case for practical boundary conditions in lattice towers. Besides, attention was paid to creating real three-dimensional [three-dimensional (3D)] hinges in the laboratory to avoid any rotation restraints, these pins were positioned in the center of each endplate [**Figs. 4**(e) and **5**(e)]. However, one test (SBU3) was conducted with one clamped support to ensure that the numerical model used later in the study was valid for other support conditions. During the experimental tests, a compressive load was applied at the center of gravity for SBE specimens. For SBU specimens, the compressive load was applied through the gravity center of the L70 × 70 × 7 angle section (the taller leg of the SBU specimens). Consequently, the SBU specimens were subjected to a combined axial force and a major axis bending moment M_u, which made it possible to consider the bending moment's influence on the results. Each connection between the two chords consisted of two batten plates, each connected with two bolts per chord (see **Figs. 4**, **5**, and **15**). The geometry of the batten plate connections for the two specimen typologies are shown in **Figs. 4**(c) and **5**(c), respectively.

The main parameters of the tested specimens are listed in **Table 1**. For intermediate connections and for the endplates on which the specimens were welded, the connection details are shown in **Figs. 4** and **5**. Endplates with identical dimensions were used to allow the laboratory technician to easily place the specimens in their intended positions.

Based on the angle section size, the batten plates were bolted with M12 (connection between L60 × 60 × 6 and batten plate) or M16 (connection between L70 × 70 × 7 and batten plate) high resistance (HR) bolts according to EN 14399-3 (CEN 2015) [**Figs. 4** (d) and **5**(d)] to create star-battened sections. The position of the applied load did not change; however, for SBU specimens, load eccentricity was obtained by an offset of the specimen location on the endplates [**Fig. 5**(b)].

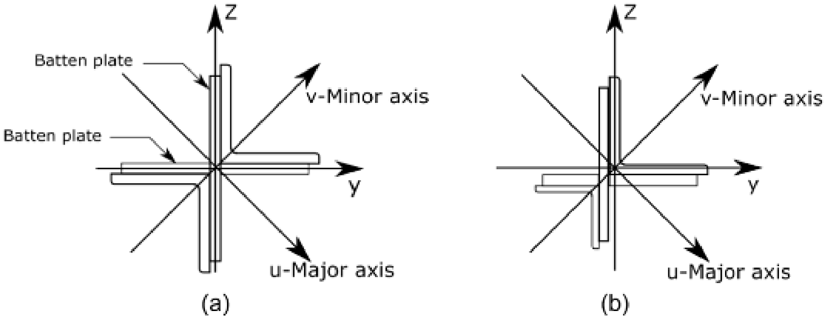

Fig. 3. The two tested configurations of closely spaced built-up members: (a) SBE; and (b) SBU.

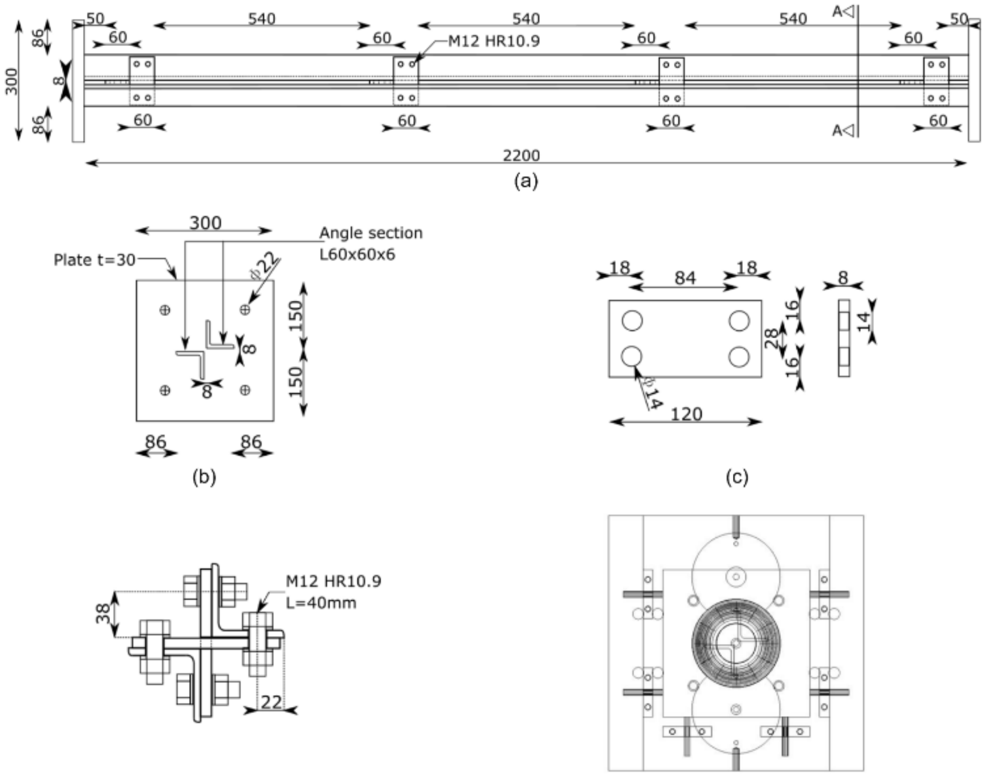

Fig. 4. Connection details for SBE specimens: (a) global view of SBE specimens (SBE1); (b) endplates, Section A-A; (c) batten plates; (d) bolted connections between the chords; and (e) position of the spherical pin.

The percentage of bolt preloading given in Table 1 refers to the nominal value for full preloading [**Eq. (1)**] equal to

$$F_{p,C} = 0{,}7 f_{ub} A_s \qquad (1)$$

where $F_{p,C}$ = nominal value for full preloading; f_{ub} = ultimate tension resistance of the bolt steel material (1,000 MPa for bolts of class 10.9); and A_s = stress area of the bolts. As shown in **Table 1**, for some bolts, the tightening torque was calculated considering 100% of $F_{p,C}$ (fully preloaded bolts); for others, the tightening torque was calculated considering 10% of $F_{p,C}$ (partially preloaded bolts). This was done in order to quantify the impact of the preloading on stability behavior. The preloading was applied by an experienced technician using Facom torque wrenches (Facom, Morangis, France).

The very low value of 10% partial preloading was chosen in order to represent the lower limit of preloading that could be considered close to (or even below) snug tightening conditions.

EXPERIMENTAL TEST SETUP, TEST PROCEDURE, AND INSTRUMENTATION

The test campaign was carried out using a hydraulic test rig called Schenk Hydropuls (Darmstadt, Germany). The loading was applied by imposed displacements until the end of the test. An example of a specimen (SBU1) in the test rig is shown in **Fig. 6**.

The loading rate was 3 mm in 10 min at the beginning of the test, and the measured data were automatically recorded by the control computer. When the load approached the expected peak load (failure), the rate was reduced to 3 mm in 20 min to avoid any potential dynamic effects. This loading system was established by the laboratory staff based on their experience with such experimental tests. However, during one experimental test (SBU1), a sudden increase in the lateral displacement of the specimen occurred together with a clang. Consequently, the specimen was unloaded to roughly 20% of the compression load before reincreasing it until the end (see section "Analysis of SBU and SBE Specimens"). The laboratory was instructed to do the same for any similar events that occurred. However, this only occurred for specimen SBU1.

MEASUREMENTS BEFORE THE TESTS

ACTUAL GEOMETRIC PROPERTIES OF THE CROSS SECTIONS

The actual geometric dimensions of the cross sections were measured in the laboratory before carrying out the test campaign. The various measurements are shown in **Fig. 7**. The measurements were taken at 3 points along the length, that is, at 1/4, 1/2, and 3/4 of the total length *L*. The mean measured dimensions are reported in **Table 2**.

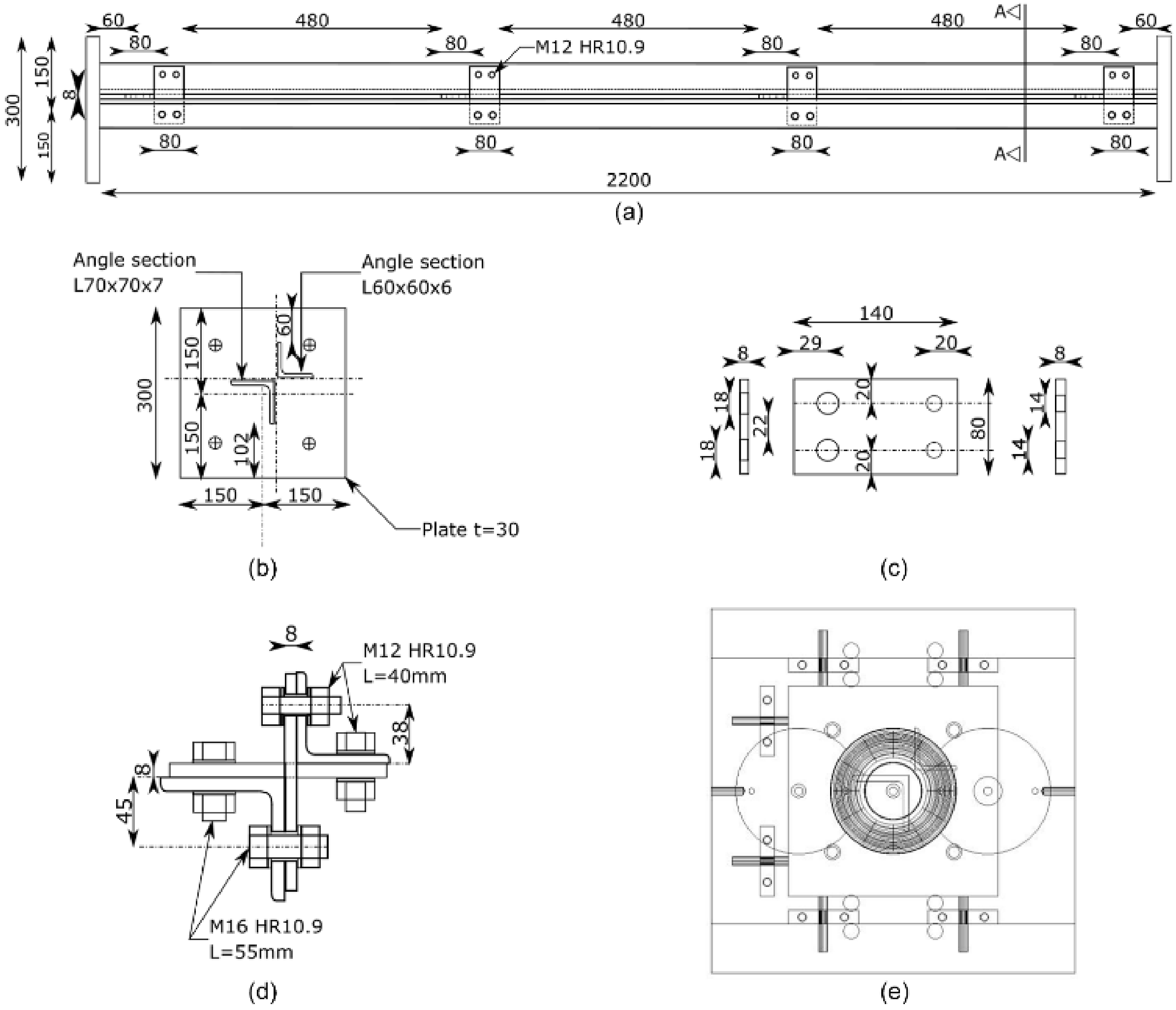

Fig. 5. Connection details for SBU specimens: (a) global view of the SBU specimens (SBU1); (b) endplates, Section A-A; (c) batten plates; (d) bolted connections between the chords; and (e) position of the spherical pin.

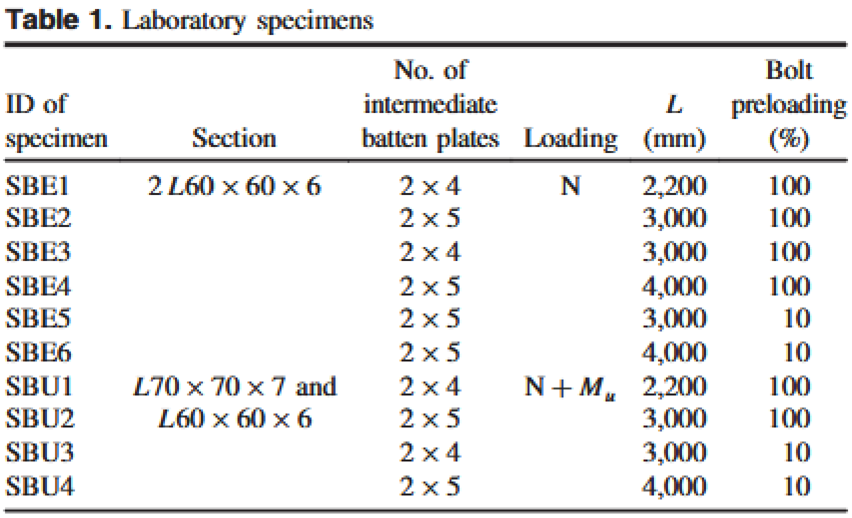

Table 1. Laboratory specimens

ID of specimen	Section	No. of intermediate batten plates	Loading	L (mm)	Bolt preloading (%)
SBE1	2 $L60 \times 60 \times 6$	2×4	N	2,200	100
SBE2		2×5		3,000	100
SBE3		2×4		3,000	100
SBE4		2×5		4,000	100
SBE5		2×5		3,000	10
SBE6		2×5		4,000	10
SBU1	$L70 \times 70 \times 7$ and	2×4	$N + M_u$	2,200	100
SBU2	$L60 \times 60 \times 6$	2×5		3,000	100
SBU3		2×4		3,000	10
SBU4		2×5		4,000	10

GEOMETRIC OUT-OF-STRAIGHTNESS

Geometric imperfection measurements were also taken before specimen testing. For each imperfection measurement, the specimen was positioned parallel to a bench equipped with a trolley carrying four laser displacement transducers, as shown in **Fig. 8**. The trolley moved along the bench, and each of the four laser displacement transducers measured the distance to the specimen.

The process was repeated with the specimen turned 90°. Hence, the initial deformation of each specimen in the two main planes was determined, as shown in **Fig. 9**. The first measurement point was located several centimeters from the intersection between the profile and the endplate. The laser measurements were not continuous but were performed in successive steps. The measurement steps depended on the positions of the bolts used to connect the batten plates. **Fig. 8** shows the trolley in the laboratory.

Two corrections were applied to the raw measurements. The first correction was performed in order to account for nonparallelism and the rotation of the measurement system given the steel members were not perfectly parallel to the setup. Moreover, even when the chariot supporting the inclinometer moved along a horizontal guiding bar, a small rotation about the longitudinal axis of the metric system was noticed. The second correction involved ensuring zero imperfection at the extremities of the column. Because there was no possibility of access for laser measurements at the member extremities due to the presence of the welded endplates, it was assumed that member imperfection was negligible in the small zones situated between the column extremities and the sections, where the first and last measurements were performed.

The geometric imperfection measurements for specimen SBU1 are shown in **Fig. 10**. The overall results of the imperfection measurements are provided in **Table 3**.

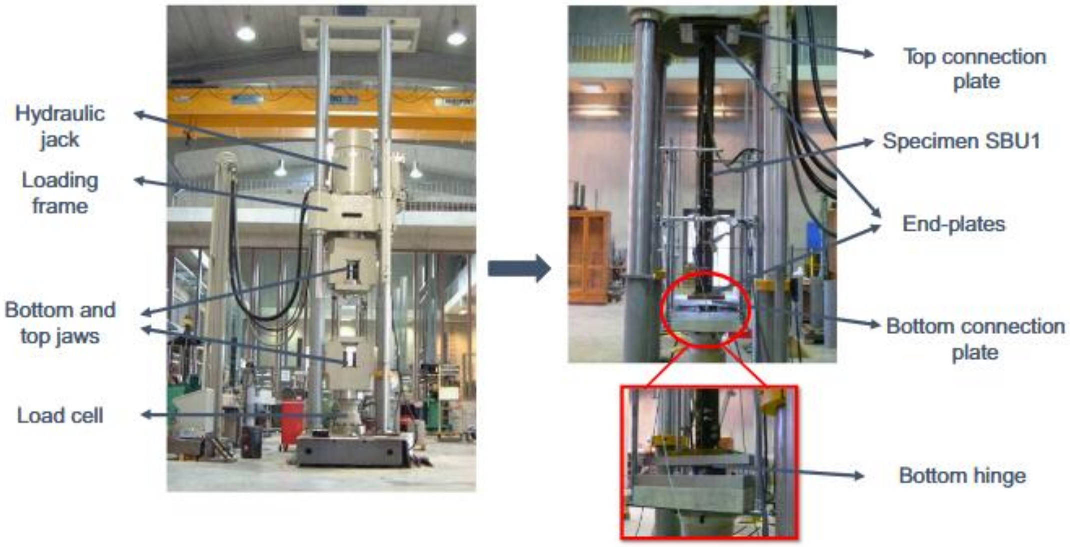

Fig. 6. Test equipment and test device with specimen SBU1.

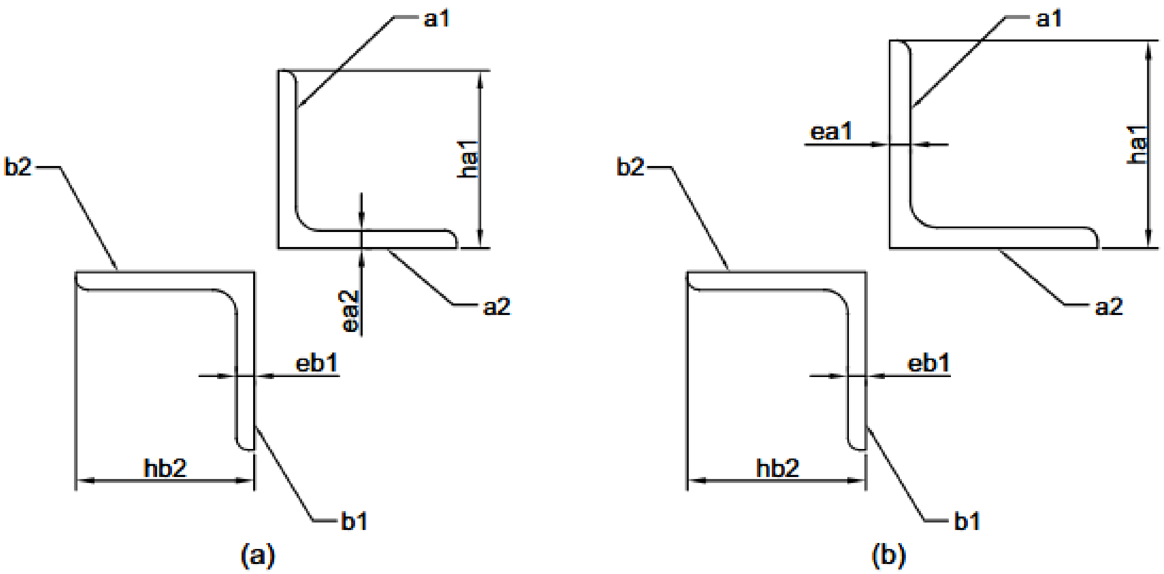

Fig. 7. Actual geometric dimensions of the cross sections: (a) SBE specimens; and (b) SBU specimens.

Table 2. Mean cross-sectional dimension measurements

	Mean dimensions (mm)					
Specimens	h_{a1}	h_{a2}	e_{a1}	e_{a2}	h_{b2}	e_{b1}
SBE1	59.73	—	—	5.82	60.40	6.05
SBE2	60.63	—	—	6.05	60.53	6.05
SBE3	60.60	—	—	6.02	59.80	5.85
SBE4	60.53	—	—	5.92	60.57	6.10
SBE5	60.53	—	—	6.05	60.87	5.91
SBE6	59.87	—	—	6.10	60.57	6.07
SBU1	69.87	—	6.93	—	59.87	6.03
SBU2	69.93	—	6.89	—	60.13	6.07
SBU3	69.90	—	6.91	—	60.37	6.01
SBU4	69.93	—	6.89	—	59.62	5.88

The location of individual measurements is indicated by the markers. For specimen SBU1, the geometric imperfection was rather low. Consequently, the measurement geometric imperfection can lead to a higher resistance compared to the generally assumed one, that is, a half-sine wave with an amplitude of *L*/1,000. Other imperfection measurement details are reported in Saufnay et al. (2020).

The maximum imperfections measured in the y, z-coordinate system were projected in the u, v-coordinate system (see **Fig. 3**) according to **Eqs. (2)** and **(3)**:

$$e_u = e_y \times \cos(45^{\circ}) - e_z \times \sin(45^{\circ}) \qquad (2)$$

$$e_v = e_y \times \sin(45^{\circ}) + e_z \times \cos(45^{\circ}) \qquad (3)$$

ECCENTRICITY

In addition, supplementary measurements were performed to check the exact position of each specimen on its end supporting plates. An eccentricity at the support may induce, during a test, a supplementary internal bending moment in a specimen. The measurements are shown in **Fig. 11**, the intended nominal values are listed in **Table 4**, and the various measurements concerning specimen locations on each endplate are shown in **Table 5**.

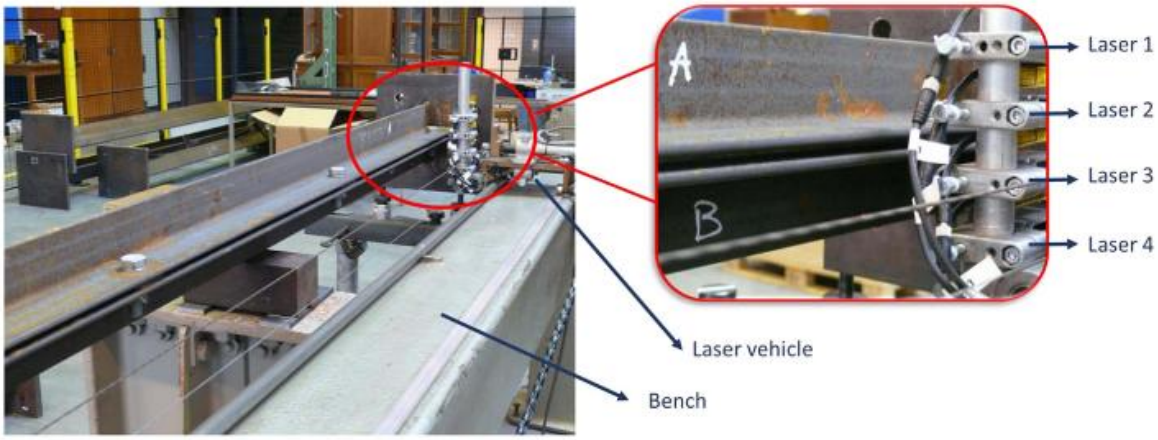

Fig. 8. Geometric imperfection measurements performed in the ULiège laboratory.

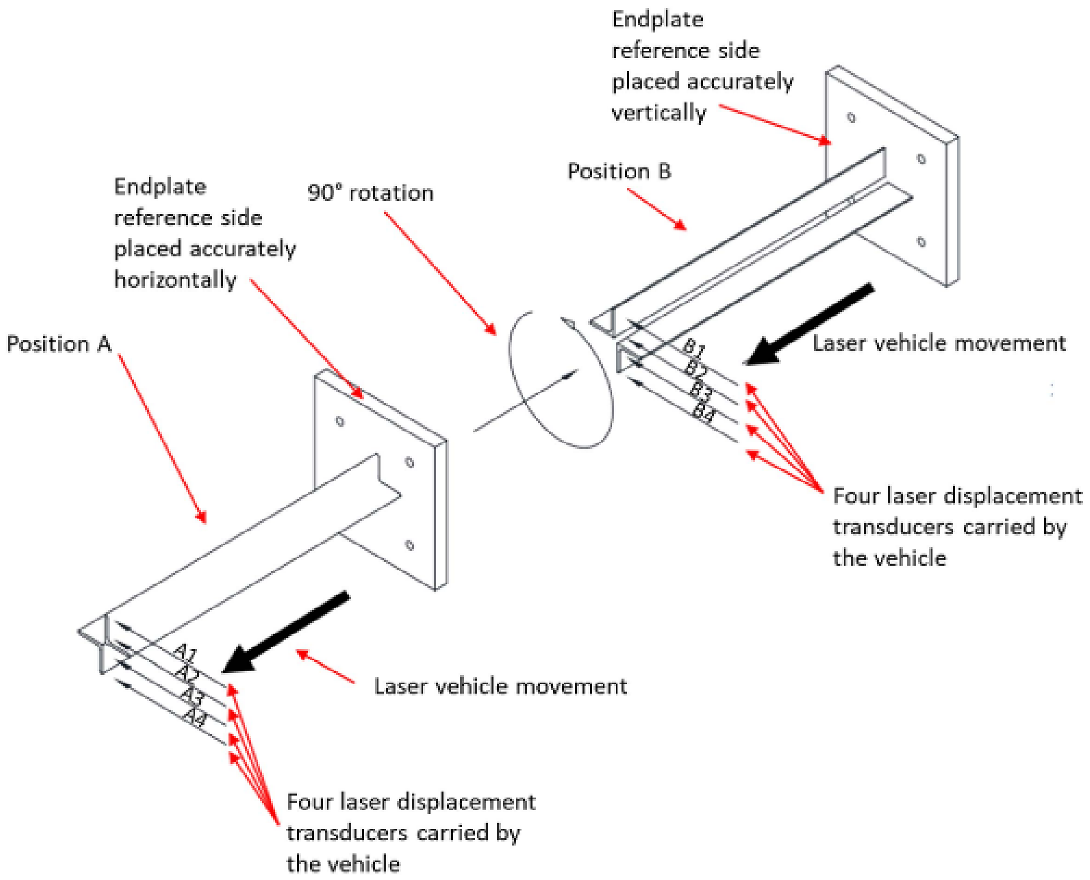

Fig. 9. Initial measurement details for star-battened sections.

MATERIAL MECHANICAL PROPERTIES

Coupon tests were performed in accordance with ISO 6892-1:2016 (ISO 2016). All in all, 12 coupon tests were carried out in this campaign. The stress-strain curves for specimen SBU4 coupon tests are shown in **Fig.** 12. The values for the other coupon tests are shown in **Table** 6, in which E = Young's modulus; R_{eh} = apparent yield strength; $R_{p0,2}$ = offset yield point, taken as the stress at which 0.2% plastic deformation occurs; and R_m = ultimate tension resistance.

Table 6 represents the mean values of the material properties for each angle section. **Table** 7 represents the material properties by angle section type. Detailed material properties are reported in Saufnay et al. (2020).

MEASUREMENTS DURING THE TESTS

During the tests, displacements and strain evolutions in the cross sections were recorded to accurately analyze the stability behavior of the tested specimens. The displacements were measured at midheight. The strain gauges that were used to record the section strains were placed at three intermediate positions along the length, that is, 1/4, 1/2, and 3/4 of the total length. The strain gauges were placed at the leg tips. **Fig. 13** illustrates both types of measurements.

The displacement transducers and strain gauges were positioned differently depending on the specimen category. The various positions, depending on the specimen category, are shown in **Fig. 14**.

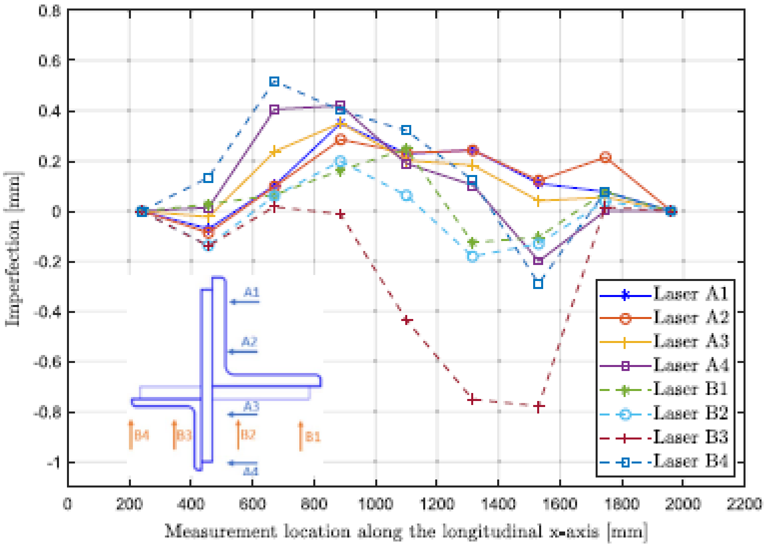

Fig. 10. Initial imperfections of the SBU1 specimen.

Table 3. Measured initial imperfections

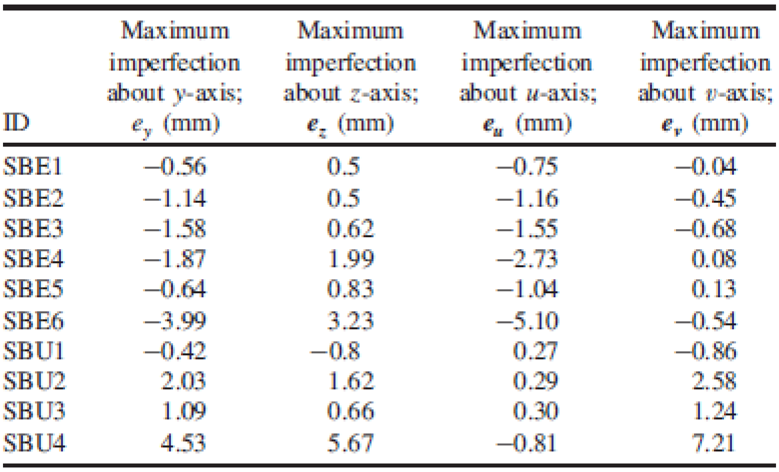

ID	Maximum imperfection about y-axis; e_y (mm)	Maximum imperfection about z-axis; e_z (mm)	Maximum imperfection about u-axis; e_u (mm)	Maximum imperfection about v-axis; e_v (mm)
SBE1	−0.56	0.5	−0.75	−0.04
SBE2	−1.14	0.5	−1.16	−0.45
SBE3	−1.58	0.62	−1.55	−0.68
SBE4	−1.87	1.99	−2.73	0.08
SBE5	−0.64	0.83	−1.04	0.13
SBE6	−3.99	3.23	−5.10	−0.54
SBU1	−0.42	−0.8	0.27	−0.86
SBU2	2.03	1.62	0.29	2.58
SBU3	1.09	0.66	0.30	1.24
SBU4	4.53	5.67	−0.81	7.21

Numerical Model and Assumptions

GEOMETRIC MODELING

To represent the mechanical behavior of the built-up member as precisely as possible, the sections, batten plates, bolts, endplates, and load introduction were explicitly modeled using finite elements of type SOLID 186 in the ANSYS element library. This type of solid element possesses 20 nodes (eight corner nodes and 12 midside nodes) with three degrees of freedom each (three translations). A global view of a finite-element model of an SBE specimen is shown in **Fig. 15**. The modeling of SBU specimens was carried out in a similar fashion.

The use of a complete solid finite-element model had the advantage that all contact regions could be explicitly modeled. **Fig. 16** shows, for an SBE specimen, the contact regions that were accounted for. Because the cutting plan does not cross the bolt hole in this figure, the contact region between the bolt shaft and the bolt hole was not explicitly represented but may be seen in **Fig. 17**. For all the contact regions, a coefficient of friction of 0.2 was considered. The contact was modeled with a pair of contact elements, CONTA174 and TARGE170, from the ANSYS element library. Both element types had eight nodes (four corner nodes and four midside nodes) with three degrees of freedom. The value of the coefficient of friction that was adopted took into account the preparation of the surface. The surfaces were only cleaned with a wire brush. Admittedly, there exists a certain tolerance (incertitude) on the real value of the coefficient of friction when this type of surface preparation is applied (the real value may be higher or lower). However, in a preliminary sensitivity study presented in Beyer et al. (2021a), it was shown that the coefficient of friction had only a small influence on the behavior and resistance of built-up members. This study also implied that the slipping of at least partially preloaded bolts does not occur during the buckling of such members, because the shear force to be transferred by the connections is rather low. The tests were also performed to verify that slipping does not occur during the buckling phenomenon.

In addition to showing the contact regions, Fig. 16 shows the cross section, the batten plates, the bolts, and the through-thickness mesh density for the sections and the batten plates. It was possible to use only one element through the thickness of the batten plates because, due to their function in the built-up members, these plates were subjected to differential stresses through their thickness. Due to the variation of axial stresses through the thickness of the legs of the angle sections, a slightly finer mesh with three elements through the thickness was necessary. In the longitudinal direction, a maximum element length of 30 mm was applied. A finer mesh was used in the connection zone (see Fig. 15). The mesh density was verified by a preliminary mesh density study showing no relevant amelioration of simulation precision when a finer mesh was used.

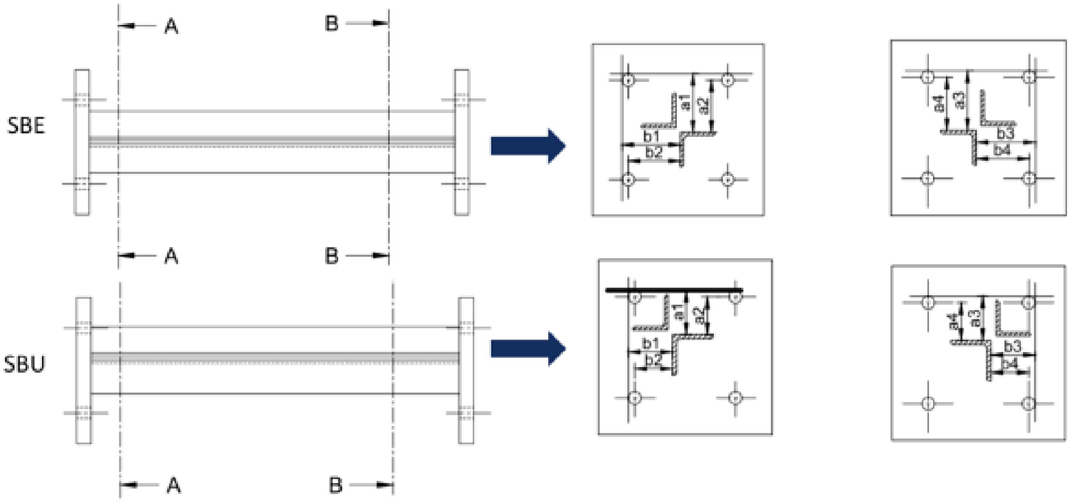

Fig. 11. Eccentricity measurements for the various tested configurations.

Table 4. Theoretical values of a_1, a_2, b_1, and b_2 of angle sections on endplates (mm)

	Bottom plate				Top plate			
Specimen	a_1	a_2	b_1	b_2	a_3	a_4	b_3	b_4
SBE	102	91	102	91	102	91	102	91
SBU	76	65	76	65	76	65	76	65

Table 5. Positioning measurements a_1, a_2, b_1, and b_2 of angle sections on endplates measured before testing (mm)

	Bottom plate				Top plate			
Specimen	a_1	a_2	b_1	b_2	a_1	a_2	b_1	b_2
SBE1	101	90	102.2	91,2	103.4	92.4	104	93
SBE2	102.4	91.4	103	92	100.3	89.3	103.8	92.8
SBE3	101.6	90.6	102	91	104.1	93.1	102.1	91.1
SBE4	104.1	93.1	101.7	90.7	101	90	103.2	92.2
SBE5	101.3	90.3	103.7	92.7	103.2	92.2	103.6	92.6
SBE6	102.6	91.6	102.8	91.8	100.5	89.5	102.3	91.3
SBU1	75.1	64.1	77	66	75.5	64.5	75.5	64.5
SBU2	75.8	64.8	73.6	62.6	73.9	62.9	73.5	62.5
SBU3	74.4	63.4	79.2	68.2	77.1	66.1	75.8	64.8
SBU4	76.5	65.5	73.8	62.8	75.7	64.7	76.3	65.3

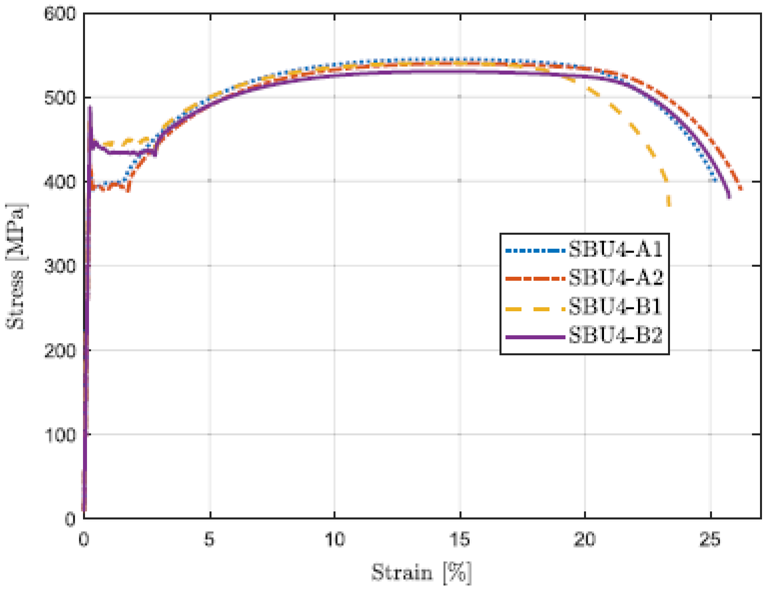

Fig. 12. Stress-strain curves for SBU4 coupon tests.

Table 6. Coupon test results

Specimen No.	Section leg	Angle section	Steel grade	E (MPa)	R_{eh} (MPa)	$R_{p0.2}$ (MPa)	R_m (MPa)
SBE4	A	$L60 \times 60 \times 6$	S355	206,703.0	485.0	444.5	545.5
	B	$L60 \times 60 \times 6$		208,742.5	476.5	443.0	536.5
SBE6	A	$L60 \times 60 \times 6$		206,329.5	479.0	444.5	542.5
SBU3	A	$L70 \times 70 \times 7$		199,047.5	414.5	393.5	542.0
SBU4	A	$L70 \times 70 \times 7$		206,991.0	416.0	392.5	542.5
	B	$L60 \times 60 \times 6$		205,092.5	479.5	445.0	535.0

The bolt hole clearance of the physical tests was considered in the connections, as shown in **Fig. 17**. The figure shows an angle leg in the numerical model. However, to easily identify the clearance, the bolt head and the washer are not represented (only the angle section and the bolt shaft are shown).

The nominal clearance in the physical tests was 2 mm; for the numerical simulations of the physical tests, it was considered that the bolt shaft was situated in the center of the bolt hole. In Beyer et al. (2021a), it was shown that the position of the bolt in a bolt hole does not affect the buckling resistance of double-angle sections.

As shown in **Table 1**, all bolts were at least partially preloaded. In the numerical model, preloading was applied through an equivalent temperature load case. This modeling was valid because the two batten plates were considered incompressible. In addition, this modeling has been frequently used; see, for example, Hu et al. (2011), Maggi et al. (2005), Nakalswamy (2010), and O'Toole et al. (2006). A differential temperature of −1,000 K was applied, and the coefficient of thermal extension α_T applied to the bolts was defined according to the intended value of the prestress. Consequently, α_T is given by **Eq. (4)**:

$$\alpha_T = \frac{F_p}{EA_s \Delta T} \qquad (4)$$

$$F_p = f_p \times F_{p,c} = f_p \times 0{,}7 A_s f_{ub} \qquad (5)$$

where F_p = intended value of the preloading given by **Eq. (5)**; f_p = applied fraction of the nominal preloading (10% or 100%); $F_{p,c}$ = nominal value of bolt preloading according to EN 1993-1-8 (CEN 2005c), clause 3.6.1 (2), and **Eq. (1)** (A_s = area of the bolt shaft; and f_{ub} = ultimate tension resistance of the bolt (bolts of class 10.9 were used; f_{ub} = 900 MPa).

After applying the differential temperature to the bolts, a static analysis was performed with the numerical model, without any other loading. The forces in the bolts were determined in a second step in order to verify the correctness of the applied approach, that is, the numerically obtained preloading compared to the intended value.

MATERIAL LAW AND IMPERFECTIONS

The numerical simulations presented in the following were based on the measured material law. The average values of Young's modulus, yield stress, and ultimate tension resistance were used. The measured stress-strain relationship was represented by a multilinear model closely following the curves shown in Fig. 12. The stress-strain values were converted in a second step before running the numerical simulations into the true stress-strain relation given by **Eqs. (6)** and **(7)**. However, this conversion was not applied to the linear elastic part of the material model

$$\sigma_{\text{true}} = \sigma(1+\varepsilon) \qquad (6)$$

$$\varepsilon_{\text{true}} = \ln(1+\varepsilon) \qquad (7)$$

where σ_{true} = true stress used in the calculation; σ = measured (engineering) stress; ε_{true} = true strain used in the calculation; and ε = measured (engineering) strain.

Table 7. Material properties by angle section type

Angle section	E (MPa)	R_{eh} (MPa)	$R_{p0.2}$ (MPa)	R_m (MPa)
$L60 \times 60 \times 6$	206,716.9	480.0	444.2	539.9
$L70 \times 70 \times 7$	203,019.3	415.3	393.0	542.3

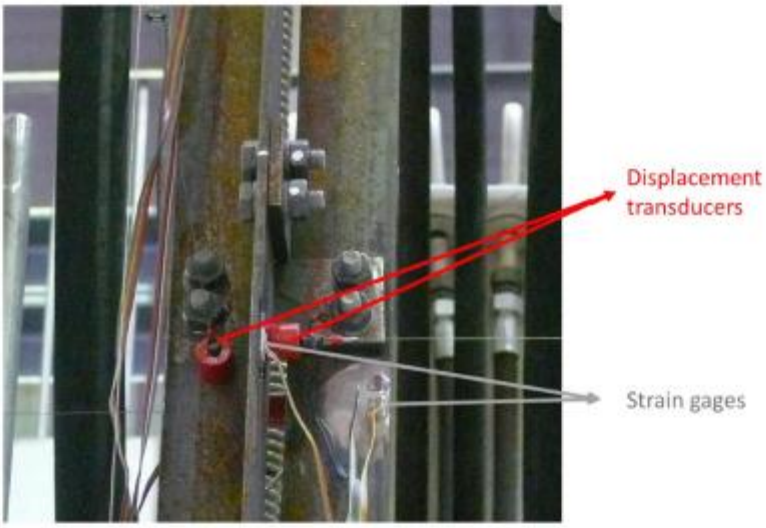

Fig. 13. General overview of measurements during specimen tests.

The cross-sectional dimensions and the position of the angle sections on the endplates were defined based on the measurements. Residual stress patterns were selected for the numerical simulations according to previous research (Može et al. 2014; Zhang and Jaspart 2013) in which appropriate measurements on similar sections and steel grades were performed. Similar measurements have also been published in a previous reference (Tebedge and Tall 1974). The residual stress pattern and the resulting residual stresses for specimen SBE2 are shown in **Fig. 18**. In the numerical model, the residual stresses were introduced as initial stresses with the help of the ANSYS command "inistate." This command allows a user to attribute an initial stress to each node. Because the initial stress state may not be perfectly equilibrated, a static analysis without external loading was performed after the definition of the initial stresses, producing the distribution shown in **Fig. 18(b)**. The resulting distribution corresponded well to the intended residual stress pattern shown in **Fig. 18(a)**.

Last, geometric imperfections were applied according to the experimentally measured values (see **Table 3**). Because the geometric imperfections were not measured continuously in the laboratory but on several points along the member length, the values of the geometric deviations defined in the numerical model corresponded to a linear interpolation between two points of measure. Consequently, the real geometric imperfections were realistically represented in the numerical simulations both in terms of shape and amplitude. The shape corresponded in general to a combination of flexural deviations and torsional deviations of a perfectly straight member.

Experimental and Numerical Results

EXPERIMENTAL TEST RESULTS

The main results are reported in this paper, but more details concerning the test results—including all load-displacement curves, strain gauges, and geometric and material properties can be found for each specimen in the deliverable 3.2 of the European project (Saufnay et al. 2020).

SBE SPECIMENS

The experimental test results for the SBE specimens are shown in **Table 8**. This table also provides the critical axial loads calculated according to **Eqs. (8)–(10)**. However, these values are theoretical, because it was supposed that the built-up members behaved as homogenous columns without any effects resulting from the connections. This was assumed because the final objective of the study was to determine the influence of the connections, which was not completely known. In addition, the warping contribution for the torsional buckling load was neglected, because the warping constant for angle sections is negligibly low.

The determination of more appropriate equations for critical axial loads, specifically considering the influence of connections, was part of the study; however, the developments will be presented in a future paper.

From the results reported in **Tables 8** and **9**, it can be concluded that the torsional buckling mode did not become relevant, because the associated critical axial load was in all cases (with the exception of SBE1) higher than the critical flexural buckling load.

For specimen SBE1, torsional buckling could potentially become relevant, but the observed failure mode indicated flexural buckling about the u-axis. This observation was also made for single angle section members in Bezas et al. (2021, 2022). Indeed, although torsional flexural buckling could be relevant based on elastic critical forces for a defined specimen, flexural buckling modes can develop due to the complex behavior of angle sections. This behavior was also studied analytically in Beyer et al. (2021b)

$$N_{cr,u} = EI_u\left(\frac{\pi}{L_{cr,u}}\right)^2 \qquad (8)$$

$$N_{cr,v} = EI_v\left(\frac{\pi}{L_{cr,v}}\right)^2 \qquad (9)$$

where $N_{cr;v}$ and $N_{cr;u}$ = elastic critical axial forces for buckling about the v- and u-axes; $N_{cr;T}$ = elastic critical axial force for torsional buckling; E = Young's modulus; G = shear modulus; I_u = second moment of area about the u-axis (major axis); I_v = second moment of area about the v-axis (minor axis); I_p = polar second moment of area (I_p ¼ I_u þI_v); I_T = torsion constant; and $L_{cr;v}$ and $L_{cr;u}$ = buckling lengths about the v- and u-axes.

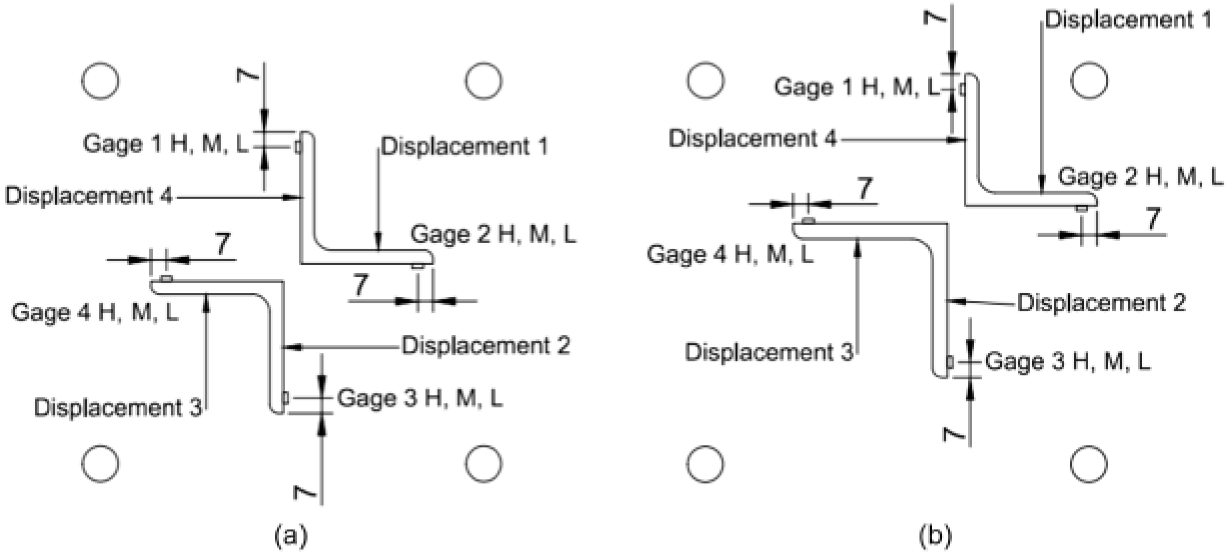

Fig. 14. Displacement transducers and strain gauges by specimen category: (a) SBE specimens; (b) SBU specimens.

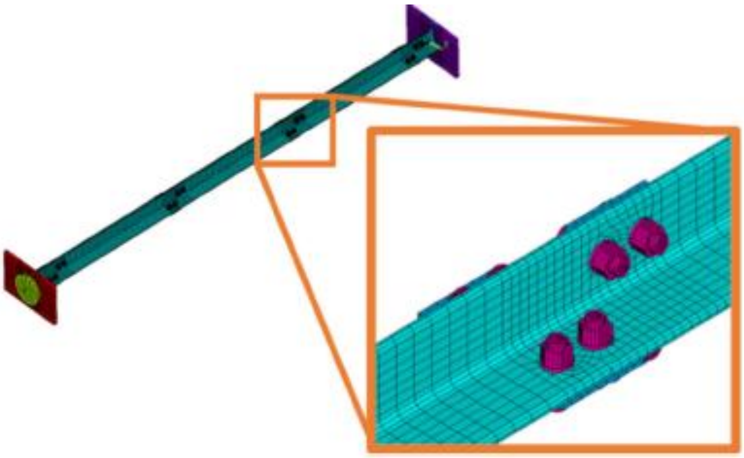

Fig. 15. Finite-element model of an SBE specimen.

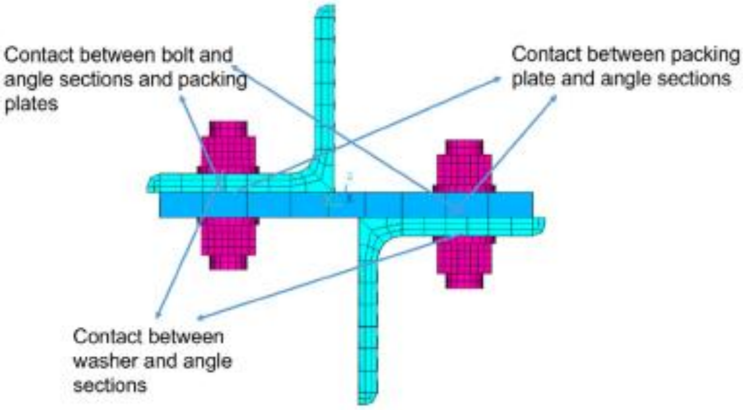

Fig. 16. Contact regions in the finite-element models and through thickness modeling of the built-up member.

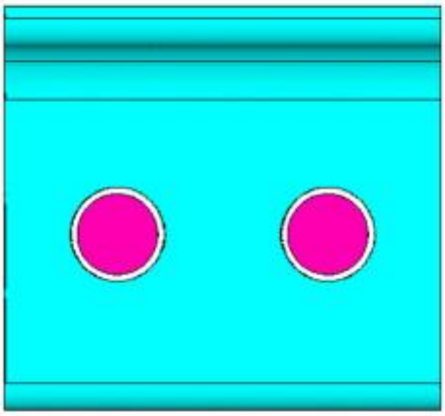

Fig. 17. Two bolt shafts and holes with clearance.

A bifurcation phenomenon appeared in most of the tested specimens. This can be explained by the fact that the absolute value of the imperfection was very low. Indeed, the imperfection value was far below the classical initial imperfection (*L*/1,000) assumed, for example, for numerical simulations for such specimens, especially about the buckling (v-) axis.

As can be illustrated in the section "Analysis of SBU and SBE Specimens," major axis displacements suddenly increased after the peak load was reached for most SBE specimens (SBE3 to SBE6). For specimens SBE1 and SBE2, a slightly different behavior was observed. For these two specimens, displacements increased about the y-axis without remarkable displacements about the u- or v-axes. Close to failure, u- respectively v-axis displacements developed abruptly, indicating a failure close to bifurcation.

Table 8 also indicates that, surprisingly, the failure loads were higher than the lowest elastic critical load linked to minor (v-) axis buckling. However, the failure loads were generally lower than the elastic critical buckling load for the observed failure mode. Failure about the major axis was observed in most cases, because the imperfection about the minor axis was very low. Consequently, failure of the specimens was observed about the axis with the highest imperfection amplitude. Specimen SBE2 was an exception. After the peak load, the displacements indicated minor axis flexural buckling. The failure load, therefore, was higher than the elastic critical load linked to this failure mode. However, this was explained previously—before the failure load was reached, the displacements increased about the y-axis (the axis parallel to the leg of the angle section); consequently, the minor axis failure mode was not mobilized before the peak load was reached. With the development of minor axis displacement, the member failed abruptly by bifurcation.

SBU SPECIMENS

Table 9 addresses the experimental test results for SBU specimens. The particularity of this specimen category was the compression load eccentricity. Due to this eccentricity, the SBU specimens were subjected to combined compression and bending; other specimens were subjected to compression only.

Despite the low amplitude of the initial imperfections, load eccentricity favored the appearance of classical flexural buckling; consequently, a bifurcation phenomenon (as was observed for the SBE specimens) was not identified for the SBU specimens. In all cases, flexural buckling about the major axis (u-axis) was observed as a result of the applied bending moment. In addition, a rather significant initial imperfection was noticed along the v-axis, which favored buckling instability about the u-axis (see **Table 3**).

NUMERICAL RESULTS—VALIDATION OF THE FINITE-ELEMENT MODEL

GENERAL

Table 10 presents a comparison between the numerical simulations and the laboratory tests. The numerical model appears to be suitable for representing the experimental behavior. A slight difference in failure mode was observed for specimen SBE2.

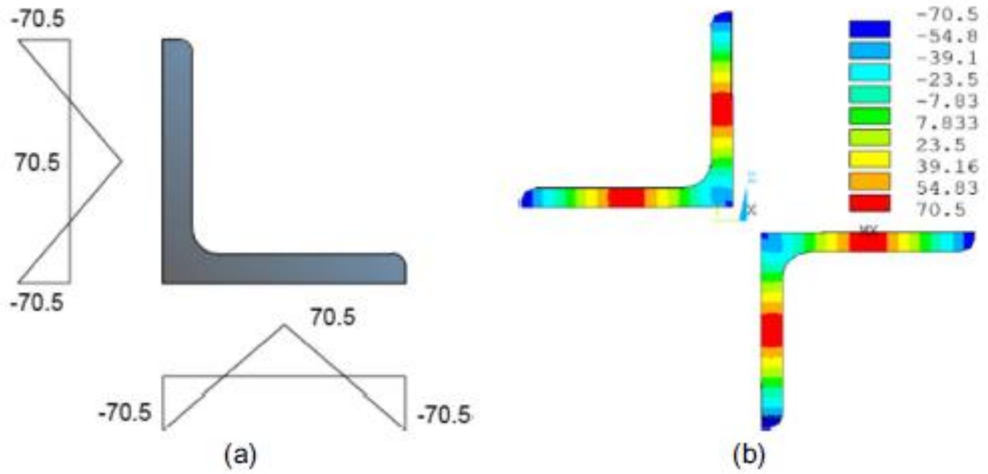

Fig. 18. Residual stresses for angle sections : (a) model pattern; and (b) residual stresses applied to specimen SBE2.

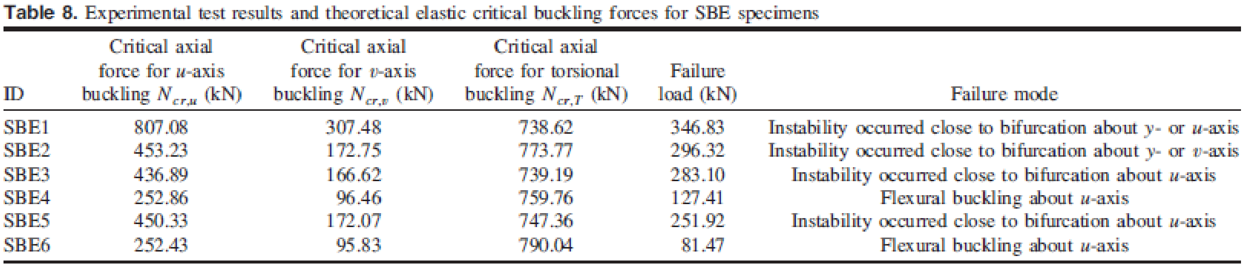

Table 8. Experimental test results and theoretical elastic critical buckling forces for SBE specimens

ID	Critical axial force for u-axis buckling $N_{cr,u}$ (kN)	Critical axial force for v-axis buckling $N_{cr,v}$ (kN)	Critical axial force for torsional buckling $N_{cr,T}$ (kN)	Failure load (kN)	Failure mode
SBE1	807.08	307.48	738.62	346.83	Instability occurred close to bifurcation about y- or u-axis
SBE2	453.23	172.75	773.77	296.32	Instability occurred close to bifurcation about y- or v-axis
SBE3	436.89	166.62	739.19	283.10	Instability occurred close to bifurcation about u-axis
SBE4	252.86	96.46	759.76	127.41	Flexural buckling about u-axis
SBE5	450.33	172.07	747.36	251.92	Instability occurred close to bifurcation about u-axis
SBE6	252.43	95.83	790.04	81.47	Flexural buckling about u-axis

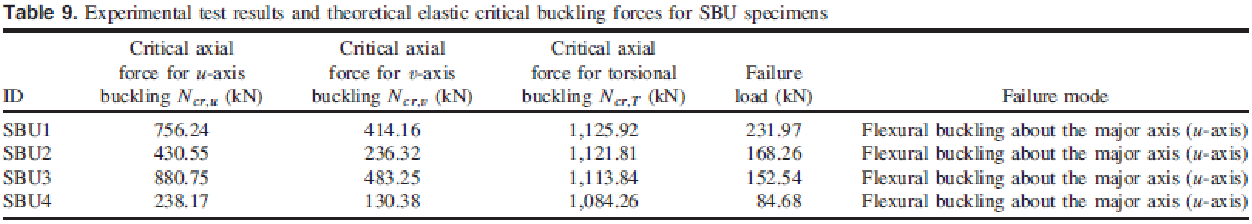

Table 9. Experimental test results and theoretical elastic critical buckling forces for SBU specimens

ID	Critical axial force for u-axis buckling $N_{cr,u}$ (kN)	Critical axial force for v-axis buckling $N_{cr,v}$ (kN)	Critical axial force for torsional buckling $N_{cr,T}$ (kN)	Failure load (kN)	Failure mode
SBU1	756.24	414.16	1,125.92	231.97	Flexural buckling about the major axis (u-axis)
SBU2	430.55	236.32	1,121.81	168.26	Flexural buckling about the major axis (u-axis)
SBU3	880.75	483.25	1,113.84	152.54	Flexural buckling about the major axis (u-axis)
SBU4	238.17	130.38	1,084.26	84.68	Flexural buckling about the major axis (u-axis)

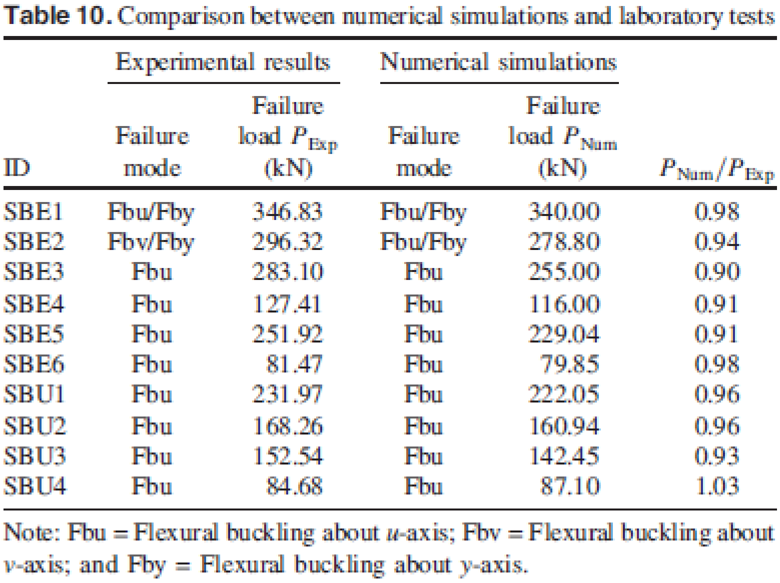

Table 10. Comparison between numerical simulations and laboratory tests

	Experimental results		Numerical simulations		
ID	Failure mode	Failure load P_{Exp} (kN)	Failure mode	Failure load P_{Num} (kN)	$P_{\mathrm{Num}}/P_{\mathrm{Exp}}$
SBE1	Fbu/Fby	346.83	Fbu/Fby	340.00	0.98
SBE2	Fbv/Fby	296.32	Fbu/Fby	278.80	0.94
SBE3	Fbu	283.10	Fbu	255.00	0.90
SBE4	Fbu	127.41	Fbu	116.00	0.91
SBE5	Fbu	251.92	Fbu	229.04	0.91
SBE6	Fbu	81.47	Fbu	79.85	0.98
SBU1	Fbu	231.97	Fbu	222.05	0.96
SBU2	Fbu	168.26	Fbu	160.94	0.96
SBU3	Fbu	152.54	Fbu	142.45	0.93
SBU4	Fbu	84.68	Fbu	87.10	1.03

Note: Fbu = Flexural buckling about u-axis; Fbv = Flexural buckling about v-axis; and Fby = Flexural buckling about y-axis.

ANALYSIS OF SBU AND SBE SPECIMENS

Fig. 19 compares the load-displacement paths obtained through numerical simulations with the results obtained in the laboratory for SBU specimens. Not only the peak load but also the evolution of the displacements was very well predicted by the developed numerical model.

Due to the eccentrically applied axial force (application point = centroid of taller angle section), buckling about the major axis was initiated, as can be observed in **Fig. 20**. Even if the direction of the displacement vectors is not exactly the same for the four configurations, one may easily conclude that the displacements are characteristic for major axis buckling. The extension of the yield zone depended on the member's slenderness. The yield zone at failure for the least slender member SBU1 is much longer that the yield zone for specimen SBU2. SBU4 failed in the elastic range due to its high slenderness. The case of specimen SBU3 is interesting; this specimen was tested with one clamped support at its lower extremity and a hinged upper end. Consequently, as seen in **Fig. 20**, there was a slightly different failure mode. As expected, the member rotation at the bottom vanished. In addition, the maximum stresses did not appear at midspan but in the upper part of the member. The objective of this test was to examine whether the numerical model could reproduce member behavior in the case of an applied moment gradient leading to higher shear forces acting in the connections. The member response and the failure load were well represented by the numerical model, even for this more complex configuration.

The failure of the SBE specimens was mainly observed about the u-u-axis, which was unexpected, because they were loaded only by an axial compression force. The expected failure was buckling about the minor axis. For specimens SBE1 and SBE2, failure was initiated about the geometric y-y-axis [in **Figs. 21(a and b)**, the measured displacement 2 increases at the beginning of loading and only close to failure the displacements 1 for specimen SBE1 and 3 for specimen SBE2 increase]. This behavior was also reproduced in the numerical simulations. However, for specimen SBE2, the simulations predicted an increase in major axis displacements after failure, while the laboratory tests showed an increase in minor axis displacements. For this specimen, postbuckling behavior was not well represented by the numerical model. Indeed, after passing through the peak load, the physical member suffered from a sudden quasi-bifurcation along the minor axis, whereas the simulation predicted a smoother transition to major axis buckling. In addition, in the numerical simulations, the displacements were higher at failure than they were in the laboratory tests, and the displacements increased more smoothly. This more pronounced nonlinear behavior may have resulted from differences in the residual stress distribution (yielding may have been initiated later in the laboratory tests) and from differences in the connection stiffnesses. Bolts may have been in contact with the hole walls in the physical specimens, whereas a nominal clearance was considered in the numerical specimens.

It is also interesting to compare the results for specimens SBE4 and SBE6. The behavior of these specimens was similar, but SBE4 had an almost 50% higher failure load than specimen SBE6. It is unlikely that this discrepancy was solely due to the different levels of preloading. This observation highlights the influence of geometric imperfections. In specimen SBE6, geometric imperfections were nearly twice as high as they were for specimen SBE4. However, for both SBE4 and SBE6, the measured imperfection shapewas close to a half-sine wave. This unfavorable shape probably explains some of the differences between specimens SBE1, SBE2, and SBE5, for which imperfection amplitude was low and the shapes of the imperfections were more favorable (maximum values of the deformations were not situated at midspan).

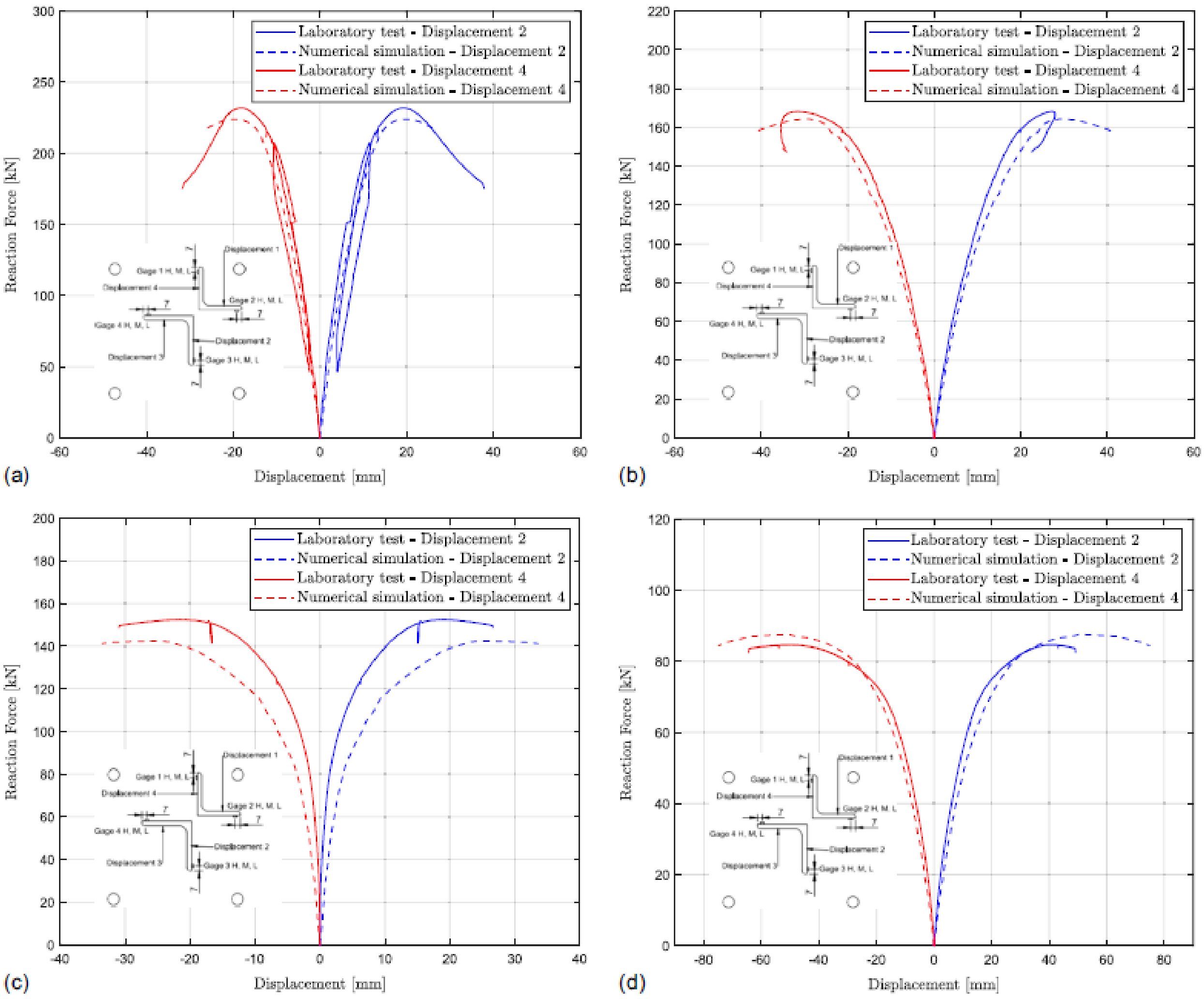

Fig. 19. Comparison between laboratory tests and numerical simulations for SBU specimens : (a) SBU1; (b) SBU2; (c) SBU3; and (d) SBU4.

Conclusions

In this study, 10 laboratory tests were conducted on closely spaced built-up members typically used in telecommunication towers or overhead line supporting towers. Two different configurations were studied: star-battened specimens with two equal sections or with two different sections. The laboratory tests were accompanied by numerical simulations in order to take a more detailed look at the mechanical behavior. The main objective of the study was the characterization of the influence of several parameters on the buckling behavior and buckling resistance of closely spaced built-up members. However, the laboratory tests showed that not only parameters such as the distance between connections or preloading in the connecting bolts had an impact on member behavior but also that the studied members were very sensitive to geometric imperfections, leading to some unexpected results. For example, one SBE specimen did not fail according to the lowest elastic buckling mode but according to the second mode (major axis buckling). This can be attributed to imperfections linked to the member (out-of-straightness) and to the load introduction (eccentricities). Due to the generally low imperfections of the laboratory specimens, most SBE specimens failed in a bifurcation mode, that is, with small displacements before failure.

Due to eccentric load application, the SBU specimens failed by flexural buckling about their major axis according to the bending moment. The applied bending moment induced the buckling direction, because its effect was more important than small geometric imperfections. Consequently, the failure mode was characterized by divergence (a smooth increase of lateral displacements before failure) rather than by bifurcation. The failure mode of SBU specimens was shown to be easily reproducible by the numerical model. The numerical model, which included measured geometric imperfections, was also able to simulate the behavior of SBE specimens failing about their major axes due to imperfections. Consequently, the numerical model will be used in ongoing work aimed at the development of a practical design procedure that can be applied to the different configurations studied in the laboratory tests. These design equations will then be proposed for the current revision of the Eurocodes to allow engineers to reliably design closely spaced built-up members.

Published in : Journal of Structural Engineering (2023), vol. 149, n°04
DOI: 10.1061/JSENDH.STENG-11642
Status : Postprint (Author's version)

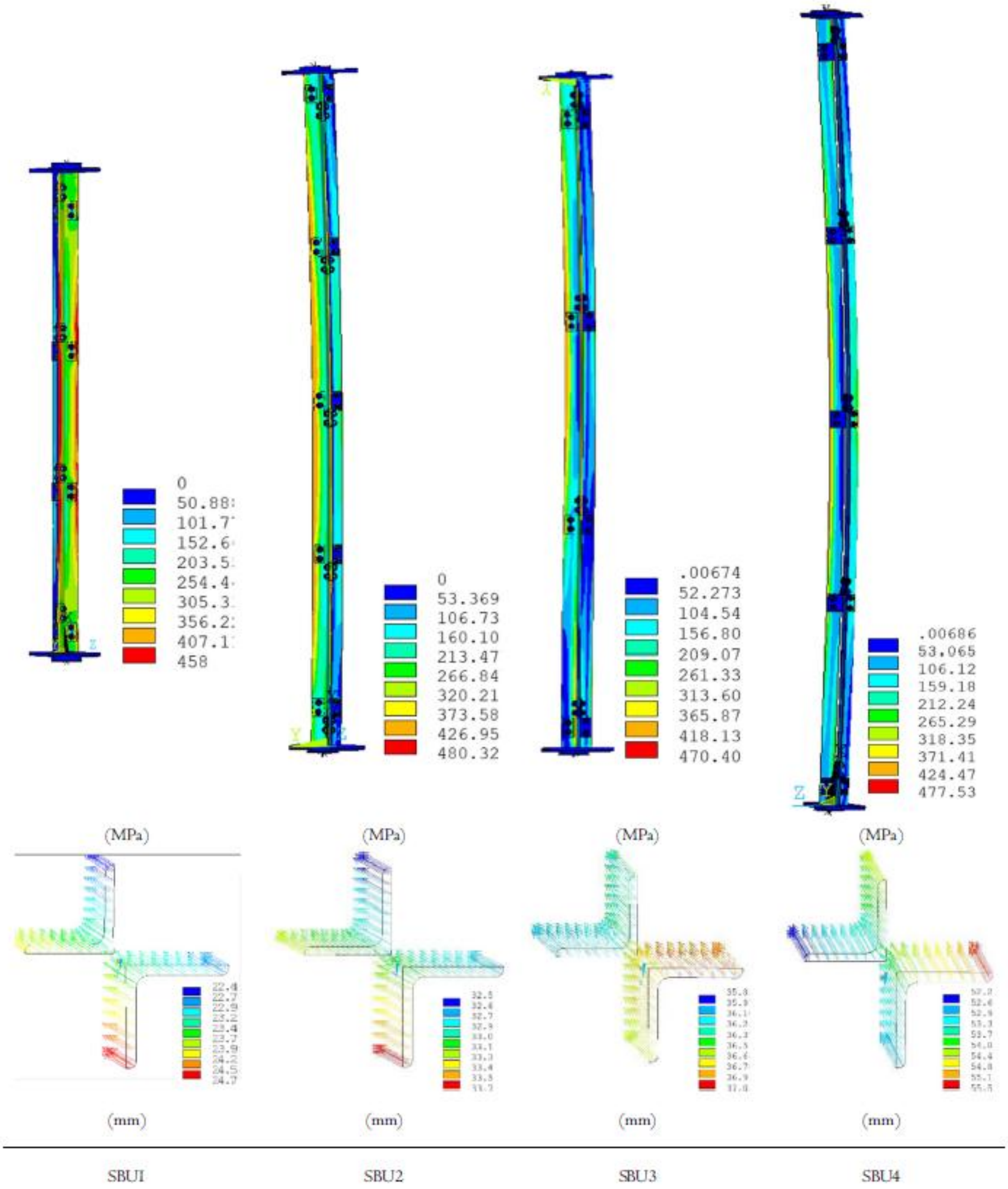

Fig. 20. Von Mises stresses and displacements at midspan for SBU specimens.

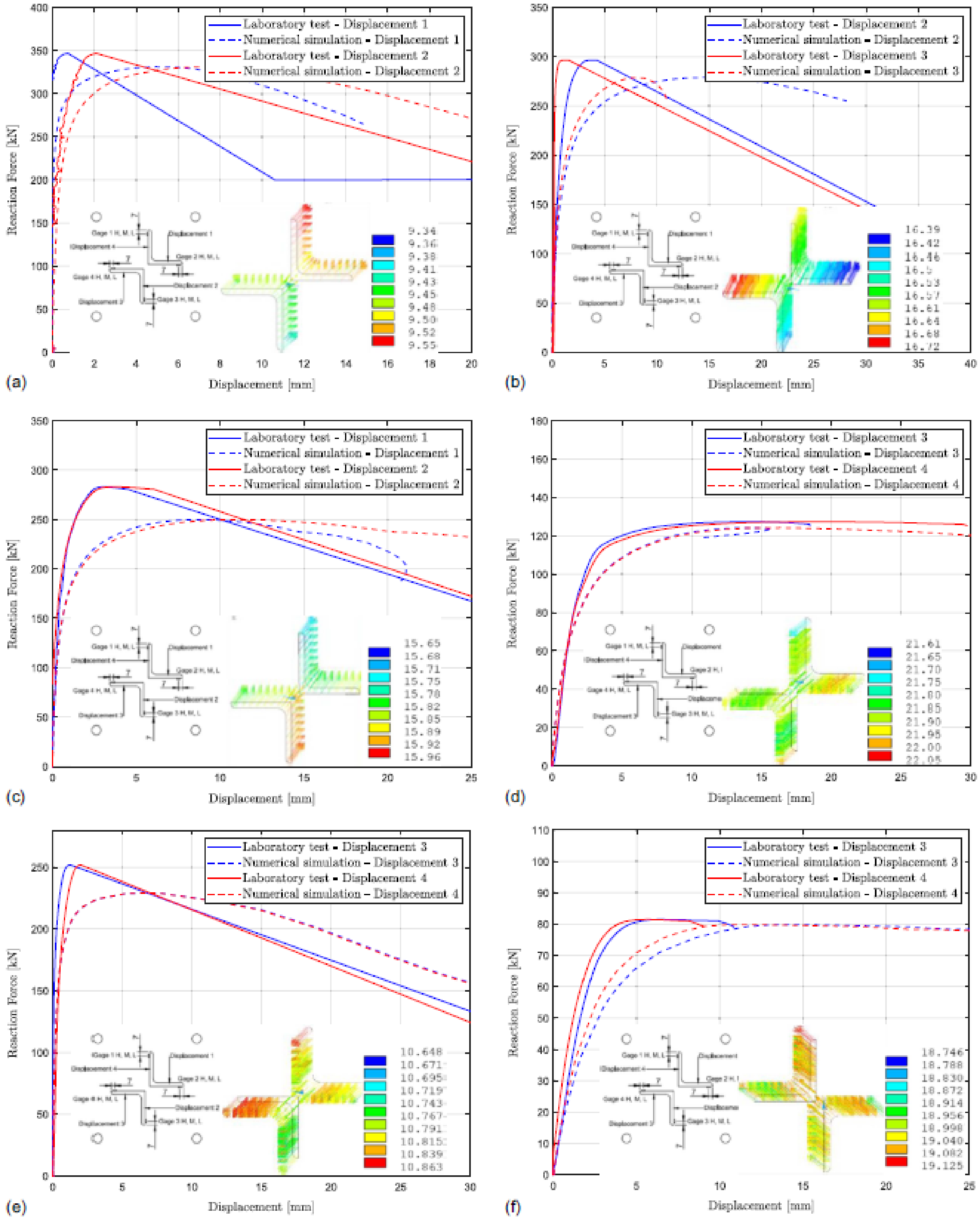

Fig. 21. Load-displacement curves and vector plot of displacements at midspan for SBE specimens: (a) SBE1; (b) SBE2; (c) SBE3; (d) SBE4; (e) SBE5; and (f) SBE6.

Data Availability Statement

Some or all data, models, or codes that support the findings of this study are available from the corresponding author upon reasonable request.

Acknowledgments

This study was carried out within the scope of work package WP3 of the European research project ANGELHY and was funded by the European Community's Research Fund for Coal and Steel (RFCS).

References

Beyer, A., A. Bureau, and J. Jaspart. 2021a. "Buckling resistance of compression members with back-to-back connected angle sections." ce/papers 4 (2–4): 2132–2139. https://doi.org/10.1002/cepa.1531.

Beyer, A., A. Bureau, J.-P. Jaspart, J.-F. Demonceau, and M.-Z. Bezas. 2021b. "Torsional, flexural and torsional-flexural buckling of angle section members—An analytical approach." In Proc., XIV Int. Conf. on Metal Structures (ICMS2021). Poznan, Poland: Taylor and Francis Group.

Bezas, M.-Z., J.-F. Demonceau, I. Vayas, and J.-P. Jaspart. 2021. "Experimental and numerical investigations on large angle high strength steel columns." Thin-Walled Struct. 159 (Feb): 107287. https://doi.org/10 .1016/j.tws.2020.107287.

Bezas, M.-Z., J.-F. Demonceau, I. Vayas, and J.-P. Jaspart. 2022. "Design rules for equal-leg angle members subjected to compression and bending." J. Constr. Steel Res. 189 (Feb): 107092. https://doi.org/10.1016/j .jcsr.2021.107092.

Botelho, I. S., P. C. G. da Silva Vellasco, L. R. O. de Lima, M. C. Rodrigues, and A. T. da Silva. 2019. "An assessment of starred rolled stainless steel angle columns." In Proc., 9th Int. Conf. on Steel and Aluminium Structures. Newport, RI: American Institute of Aeronautics and Astronautics.

CEN (European Committee for Standardization). 2005a. Design of steel structures—Part 1-1: General rules and rules for buildings. EN 1993-1-1. Brussels, Belgium: CEN.

CEN (European Committee for Standardization). 2005b. Design of steel structures part 1-4: General rules—Supplementary rules for stainless steels. EN 1993-1-4, Eurocode 3. Brussels, Belgium: CEN.

CEN (European Committee for Standardization). 2005c. Design of steel structures—Part 1-8: Design of joints. EN1993-1-8. Brussels, Belgium: CEN.

CEN (European Committee for Standardization). 2015. High-strength structural bolting assemblies for preloading—Part 3: System HR–Hexagon bolt and nut assemblies. EN 14399-3. Brussels, Belgium: CEN.

Elchalakani, M. 2016. "Rehabilitation of corroded steel CHS under combined bending and bearing using CFRP." J. Constr. Steel Res. 125 (Oct): 26–42. https://doi.org/10.1016/j.jcsr.2016.06.008.

Hu, Y. C., Y. Z. Hu, H. X. Li, and J. Y. Hou. 2011. "Research on loading simulation of bolt preload in finite element analysis based on ANSYS." Adv. Mater. Res. 156 (Oct): 615–620. https://doi.org/10.4028/www .scientific.net/AMR.156-157.615.

ISO. 2016. Metallic materials—Tensile testing—Part 1: Method of test at room temperature. ISO 6892-1. Geneva: ISO.

Kitipornchai, S., and H. W. Lee. 1986. "Inelastic experiments on angle and tee struts." J. Constr. Steel Res. 6 (3): 219–236. https://doi.org/10.1016 /0143-974X(86)90035-0.

Lu, C., X. Ma, and J. E. Mills. 2015. "Modeling of retrofitted steel transmission towers." J. Constr. Steel Res. 112 (Sep): 138–154. https://doi .org/10.1016/j.jcsr.2015.04.005.

Maggi, Y. I., R. M. Gonçalves, R. T. Leon, and L. F. L. Ribeiro. 2005. "Parametric analysis of steel bolted end plate connections using finite element modeling." J. Constr. Steel Res. 61 (5): 689–708. https://doi .org/10.1016/j.jcsr.2004.12.001.

Mills, J. E., X. Ma, and Y. Zhuge. 2012. "Experimental study on multi-panel retrofitted steel transmission towers." J. Constr. Steel Res. 78 (Nov): 58–67. https://doi.org/10.1016/j.jcsr.2012.06.004.

Može, P., L. G. Cajot, F. Sinur, K. Rejec, and D. Beg. 2014. "Residual stress distribution of large steel equal leg angles." Eng. Struct. 71 (Jul): 35–47. https://doi.org/10.1016/j.engstruct.2014.03.040.

Nakalswamy, K. K. 2010. "Experimental and numerical analysis of structures with bolted joints subjected to impact load." Doctoral dissertation, Dept. of Mechanical Engineering, Univ. of Nevada, Las Vegas.

Oszvald, K., P. Tomka, and L. Dunai. 2016. "The remaining load-bearing capacity of corroded steel angle compression members." J. Constr. Steel Res. 120 (Apr): 188–198. https://doi.org/10.1016/j.jcsr.2016.01.003.

O'Toole, B., K. Karpanan, and M. Feghhi. 2006. "Experimental and finite element analysis of preloaded bolted joints under impact loading." In Vol. 3 of Proc., 47th AIAA/ASME/ASCE/AHS/ASC Structures, Structural Dynamics, and Materials Conf. 14th AIAA/ASME/AHS Adaptive Structures Conf. 7th, 2024–2032. Newport, RI: American Institute of Aeronautics and Astronautics.

Saufnay, L., M.-Z. Bezas, J.-P. Jaspart, J.-F. Demonceau, M. Verstraete, and M. Bustos Hermosilla. 2020. 2: Report on experimental tests on closely spaced built-up members. ANGELHY-D3. Paris: Research Fund for Coal and Steel.

Selvaraj, S., M. Madhavan, S. U. Dongre, and J. Vekatesan. 2016. "Improving the flexural stiffness and lateral torsional buckling behaviour of the structural steel channel sections by CFRP strengthening." In Proc., 8th Int. Conf. on Steel and Aluminium Structures. Bradford, UK: Independent Publishing Network.

Tebedge, N., and L. Tall. 1974. "Contraintes résiduelles dans les profilés en acier—Synthèse des valeurs mesurées." Rev. Constr. Mét. 11 (2): 37–48. Timošenko, S. P. 1961. Theory of elastic stability. 2nd ed. New York: McGraw-Hill.

Timoshenko, S. P. 1913. "Stabilité des systèmes élastiques." Ann. Ponts Chaussées 3 (9): 496–566.

Tomasz, P. P., and W. Siwowski. 2016. "Flexural strengthening of steel beams with passive and active CFRP plates." In Proc., 8th Int. Conf. on Steel and Aluminium Structures. Manchester, UK: The Univ. of Manchester.

Vlachakis, K., S. Reygner, M. Tibolt, and I. Vayas. 2021. "Experimental investigations on rolled angle sections reinforced with CFRP plates." ce/papers 4 (2–4): 229–236. https://doi.org/10.1002/cepa.1286.

Wan, H., R. Feng, and Q. Chen. 2016. "Advances in the study of steel flexural members strengthened by CFRP." In Proc., 8th Int. Conf. on Steel and Aluminium Structures. Bradford, UK: Independent Publishing Network.

Yousefi, O., K. Narmashiri, A. A. Hedayat, and A. Karbakhsh. 2021. "Strengthening of corroded steel CHS columns under axial compressive loads using CFRP." J. Constr. Steel Res. 178 (Mar): 106496. https://doi .org/10.1016/j.jcsr.2020.106496.

Yu,X., H. Deng, D. Zhang, and L. Cui. 2017. "Buckling behavior of420 MPa HSSY columns: Test investigation and design approach." Eng. Struct. 148 (Oct): 793–812. https://doi.org/10.1016/j.engstruct.2017.07.016.

Zhang, L., and J. P. Jaspart. 2013. Stability of members in compression made of large hot-rolled and welded angles. Liège, Belgium: Université de Liège.